Terminal Doppler Weather Radar Retrievals in Complex Terrain During a Summer High Ozone Period

Aaron C. McCutchan, John D. Horel, and Sebastian W. Hoch

University of Utah Department of Atmospheric Sciences, Salt Lake City, Utah

Corresponding author: Aaron C. McCutchan, aaron.mccutchan@utah.edu

ABSTRACT: Out of the 45 radars comprising the Terminal Doppler Weather Radar (TDWR) network, 21 are located in areas of complex terrain. Their mission to observe low-level wind shear at major airports prone to strong shear-induced accidents puts them in an ideal position to fill critical boundary layer observation gaps within the NEXRAD network in these regions. Retrievals such as Velocity Azimuth Display and Velocity Volume Processing (VVP) are used to create time-height profiles of the boundary layer from radar conical scans, but assume that a wide area around the radar is horizontally homogeneous. This assumption is rarely met in regions of complex terrain. This paper introduces a VVP retrieval with limited radius to make these profiling techniques informative for flows affected by topography. These retrievals can be applied to any operational radar to help examine critical boundary layer processes. VVP retrievals were derived from the TDWR for Salt Lake City International Airport, TSLC, during a summertime high ozone period. These observations highlighted thermally driven circulations and variations in boundary layer depth at high vertical and temporal resolution and provided insight on their influence on air quality.

SIGNIFICANCE STATEMENT: Residents in many urban areas of the United States are exposed to elevated ozone concentrations during the summer months. In complex terrain, thermally-driven circulations and terrain-forced flows affect chemical processes by modulating mixing and transport. A novel technique to monitor local boundary layer conditions on small horizontal length scales was applied to data from the Terminal Doppler Weather Radar located near Salt Lake City International Airport during a multi-day high ozone event, and effects of these flows on ozone concentrations are illustrated. This technique can be applied to other operational weather radars to create long-term and real-time records of near-surface processes at high vertical and temporal resolution.

1. Introduction

Some of the earliest uses of radar for boundary layer studies relied on Velocity Azimuth Displays (VAD) introduced by Browning and Wexler (1968). This technique fits a sinusoid to Doppler velocity observations varying with azimuth collected at a constant range and elevation angle, then maps them in the vertical using the range-height relationship to create a wind profile. Later iterations of this method, such as the Velocity Volume Processing (VVP) and enhanced VAD, combined samples from multiple elevation angles to obtain this profile (Waldteufel and Corbin 1979; Matejka and Srivastava 1991; Boccippio 1995). The enhanced VAD forms the basis of the level-3 Vertical Wind Profile (VWP) product available to present-day NEXRAD users. Statistical properties of residuals from these profiles and other radar moments can be combined with the resulting wind profiles to derive turbulence properties (Doviak and Zrnic 1993). Principles from these retrievals were later applied to create volumetric wind fields from single radars by assimilation of Doppler velocity data into models using three-dimensional variational, four-dimensional variational and ensemble Kalman techniques (Xiao et al. 2005; Gao et al. 2013; Tong et al. 2020; Wang and Pu 2021; Bian et al. 2023).

Boundary layer depth can be derived from observing shear layers within these profiles, but methods detecting boundary layer depth in clear air by identifying clear air Bragg scattering (CABS) layers using other radar moments have also been developed. CABS at the interface of the convective boundary layer (CBL) and residual layer during quiescent periods can appear as a band of enhanced reflectivity at constant range that moves out from the radar through the morning as the mixed layer increases in depth (Rabin and Doviak 1989; Heinselman et al. 2009; Melnikov et al. 2011; Elmore et al. 2012; Davison et al. 2013). The dual polarization (dual-pol) upgrade to WSR-88D radars in the mid 2010s enabled easy distinction between Bragg, biota, and other non-meteorological targets, increasing the reliability of the moment-based boundary layer top estimate by searching for the CABS fingerprint located within the reflectivity band (Zrnic and Ryzhkov 1998; Bachmann and Zrnić 2007; Melnikov et al. 2013; Richardson et al. 2017; Chandrasekar et al. 2023). Banghoff et al. (2018) automated detection of these layers leveraging quasi-vertical profiles (QVP) which take averages of radar moments around rings of constant range and maps them using the range-height relationship, similar to a VAD (Ryzhkov et al. 2016).

The major airports of Salt Lake City, Phoenix, Las Vegas, and Denver are covered by TDWR systems that prioritize near-surface coverage (Evans and Turnbull 1989). To maximize spatial coverage around complex terrain, many WSR-88Ds in the Intermountain West are located at high elevations relative to the basin floors containing nearby urban areas. This limits their capacity to provide accurate observations of the boundary layer on the basin floor. Since the airports are co-located with population centers on the basin floor, TDWRs can be used to fill the observation gap.

Boundary layer observations in the Intermountain West are particularly useful for diagnosing processes contributing to hazardous concentrations of air pollutants. Many cities there are in non-attainment of EPA National Ambient Air Quality Standards (NAAQS) for eight-hour average ozone ($\overline{O_3}$), increasing the public's risk of acute respiratory illness and the likelihood of developing chronic respiratory conditions (Hubbell et al. 2005; Fann et al. 2012; Sousa et al. 2013). To be in attainment of NAAQS, a region must not exceed 70 ppb $\overline{O_3}$ at an official observing site more than three days in a three year period, with some allowance for exceptional events. If a region is in non-attainment, the state must submit a report to the EPA outlining policy measures they will take to reduce air pollution (Jaffe et al. 2024). Mechanisms contributing to ozone pollution are both chemical and meteorological. Improving understanding of these mechanisms and their relative contributions is key to creating effective policy.

Ozone is a secondary pollutant produced primarily by volatile organic compounds (VOCs) reacting with nitrous oxides (NO_x) in the presence of sunlight with both reactants largely coming from urban emissions (Seinfeld and Pandis 2016). The rate of these reactions increases with ambient air temperature and solar radiation intensity, thus days where maximum $\overline{O_3}$ exceeds 70 ppb, hereafter referred to as exceedance events, tend to co-occur with summer heat waves (Baier et al. 2015; Pusede et al. 2015; Coates et al. 2016).

During quiescent periods, ozone concentrations follow a diurnal cycle based on solar radiation and boundary layer structure. During the overnight hours, ozone is converted by NO into NO_2 (Seinfeld and Pandis 2016). Within the residual layer, NO is limited and as a result not all ozone is converted, however emissions of NO_x at the surface continue after sunset and are confined within the developing stable layer. This allows additional titration of ozone, and combined with the effects of deposition and halide scavenging reduces ozone near the surface to near zero by midnight (Logan et al. 1981; Simpson et al. 2007; Clifton et al. 2020). When the sun rises, CBL development and photochemical production of ozone begin. Since ozone concentrations in the residual layer are higher, mixing within the CBL initially increases ozone concentrations. The additional NO_x and VOCs in the eroding stable layer cause ozone concentrations to rise faster within the growing CBL than within the residual layer, with ozone concentrations in the CBL eventually overtaking those in the residual layer. At this point, fumigation from the growing CBL switches from increasing surface ozone to decreasing surface ozone. After solar noon, photochemical production slows down because of decreased solar radiation, and this effect combined with the ventilating effect of fumigation causes ozone values to decrease slowly throughout the afternoon. At sunset, photochemical production stops and the CBL leaves a well-mixed residual layer in its wake, setting up a repeat of the cycle (Kaser et al. 2017).

In the Intermountain West, terrain complicates the typical diurnal evolution in ozone concentration. High terrain may impede horizontal transport that often dominates in other regions (Banta et al. 2011), and the structure of the boundary layer is altered by thermally-driven wind systems (De Wekker and Kossmann 2015; Lehner and Rotach 2018). During the day, upslope and upvalley winds transport pollutants from basin floors to higher levels of the atmosphere, and at night downslope and downvalley winds bring regional concentrations of pollutants downward (Liu et al. 1992; Jaffe 2011; Chow et al. 2013; Horel et al. 2016). Additionally, much of the region is at high elevation, which increases background ozone concentrations at baseline (Brodin et al. 2010). Regional wildfire smoke transport also contributes extra precursor species (McClure and Jaffe 2018; Ninneman and Jaffe 2021; Xu et al. 2021; Rickly et al. 2023; Jaffe et al. 2024).

In Salt Lake City, Utah (SLC), the typical diurnal evolution in ozone concentration is further complicated by lake breezes from the Great Salt Lake . The boundary layer behind lake breezes can act as reservoirs of clean or polluted air that is transported as the lake breeze propagates onshore. Additionally, the convergence zone along the head of the lake breeze can concentrate urban emissions and pollutants (Zumpfe and Horel 2007; Crosman and Horel 2016; Horel et al. 2016; Blaylock et al. 2017). A similar but weaker effect has been noted on playa surfaces (Massey et al. 2017). Salt Lake and Davis counties, which comprise the greater SLC urban area, are both in moderate non-attainment of the NAAQS $\overline{O_3}$ standard. The co-location of the Great Salt Lake, SLC, and the Wasatch Mountains makes it a unique location to explore the impacts of a number of thermally driven circulations upon ozone.

Horel et al. (2016) hypothesized that the highly reflective Farmington Bay Playa (FBP), named after the arm of the Great Salt Lake that used to fill the region north of SLC and east of Antelope Island, has substantial influence upon ozone concentrations in the urban corridor between FBP and the Wasatch mountains (Fig. 1). A team from the University of Utah (UU) conducted a small field study in summer 2022 to explore ozone transport near FBP and the nearby wetlands (McCutchan 2023). The TDWR for SLC International Airport, TSLC, is located on the eastern fringe of FBP and has been key in observing lake breeze progression during prior air quality studies (Zumpfe and Horel 2007; Crosman and Horel 2016; Blaylock et al. 2017). We used TSLC in the summer study to examine thermally driven flows, playa breezes, and boundary layer depth using VVP and range-defined QVP (RD-QVP) retrievals. Applying the radar boundary layer profiling techniques introduced earlier is difficult in complex terrain as many of them rely on the assumption of large areas of horizontally uniform flow and scatterers. By limiting the horizontal retrieval radius, we improve characterizations of physical processes associated with the complicated mountain boundary layer flows. This technique can be applied to any operational weather radar and used to create long-term, real-time records of the boundary layer at high vertical and temporal resolution.

In this paper, we discuss the radar techniques used in the summer 2022 study, showcase processes we were able to observe using them, and discuss some possible impacts of those processes on observed ozone concentrations. Section 2 describes the radar methods and their verification in more detail. Section 3 introduces the technical specifications of TSLC and describes the summer

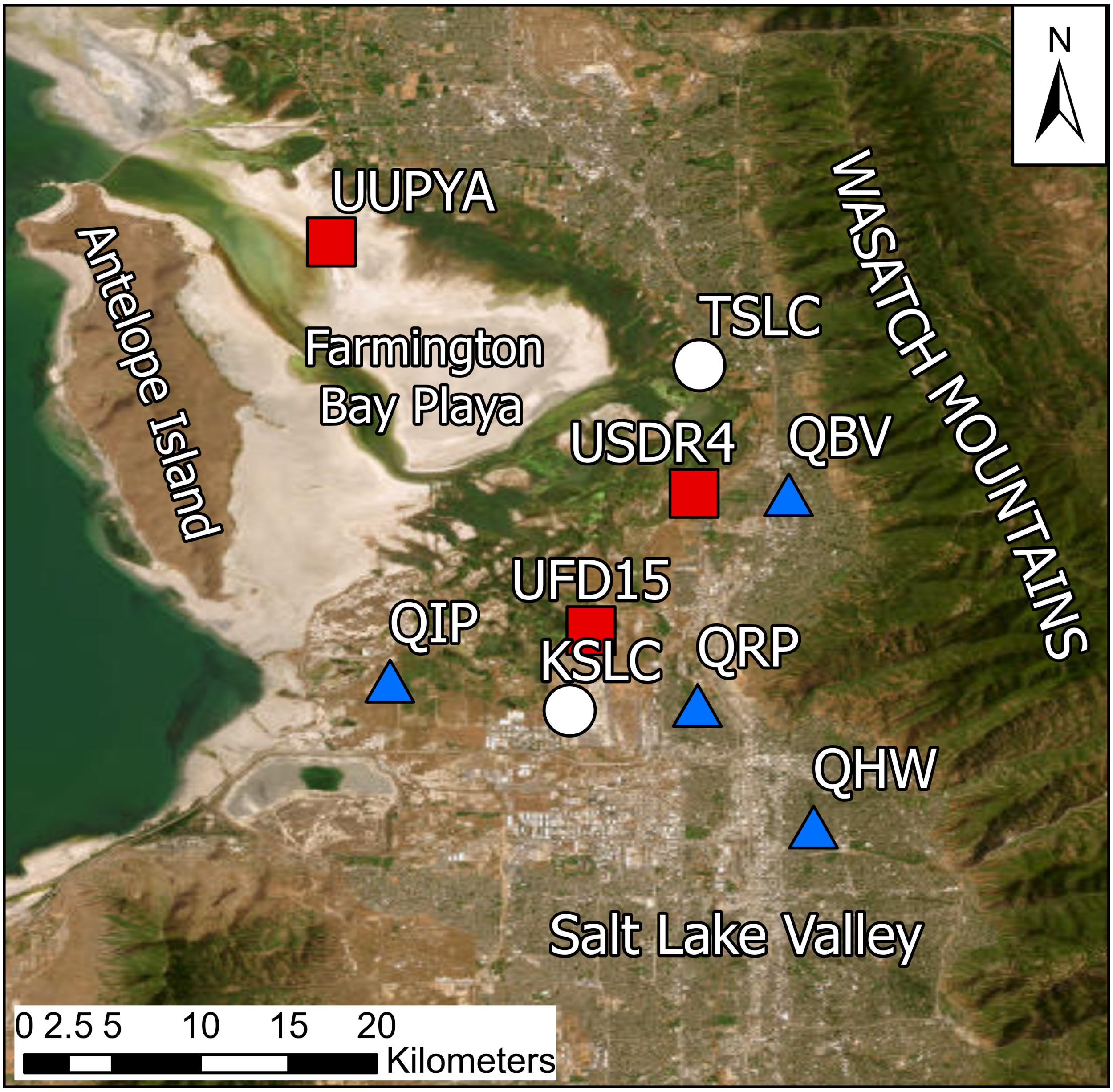

FIG. 1. Locations of key sensors for the 2022 summer ozone study and major geographic features of the Farmington Bay Playa region. Blue triangles denote Utah Division of Air Quality sensors. Red squares mark temporary University of Utah 2B Technologies ozone monitors, with additional meteorological equipment at UUPYA and UFD15. The white circles mark SLC International Airport (KSLC) and TSLC, the TDWR for the airport.

ozone study. Section 4 describes observations made with the retrievals during a ten-day high ozone event. Finally, section 5 recaps the findings and suggests directions for future work.

2. Radar Retrieval Methodology

Given an azimuth relative to north α, elevation angle ϕ, and assuming scatterers are following the mean wind, Cartesian wind components are expected to yield a radial velocity value consistent with

$$V_r = u\ sin(\alpha)cos(\phi) + v\ cos(\alpha)cos(\phi) + w\ sin(\phi)$$

Theoretically, three sufficiently orthogonal radial velocities could be used to invert this relationship and resolve Cartesian wind components. In practice, turbulence and system noise in Doppler radars and lidars create too much variance for such methods to be stable (Teschke and Lehmann 2017; Wildmann et al. 2020). Instead, Fourier transforms or least squares regression with respect to azimuth along a ring of constant range are used to derive Cartesian wind components at a given height above the radar in the VAD retrieval (Browning and Wexler 1968; Doviak and Zrnic 1993). QVP retrievals average over other radar moments on the same rings of constant range to create a profile (Ryzhkov et al. 2016).

Operational retrievals typically assume scatterers and the wind field remain uniform near the radar, often up to a radius of 50 km (Holleman 2005; Ryzhkov et al. 2016; Tobin and Kumjian 2017; Griffin et al. 2018; Hu and Ryzhkov 2022). Assuming such large uniform areas is unrealistic for radars in complex terrain. The size of the assumed uniform area can be reduced by scanning at a higher angle, decreasing vertical resolution, or only accepting a shallower profile. Effects of these tradeoffs can be reduced by combining conical scans at multiple elevation angles. The VVP does so by allowing varying elevation in addition to azimuth in the least squares regression (Waldteufel and Corbin 1979; Boccippio 1995). A cylindrical domain centered on the radar is partitioned into stacked disks, and regression is carried out over gates within a given disk to create an estimate. In addition, statistics of other moments from gates within the disk can be calculated to form a vertical profile similar to an RD-QVP (Tobin and Kumjian 2017).

For this study, we used a cylinder radius of 5 km, roughly the distance from TSLC to the nearest foothills. Disks were partitioned on a logarithmic axis with the lowest disk being 3 m deep and the highest disk 200 m deep. Validation of the retrievals at TSLC using radiosondes launched twice-daily at KSLC was undertaken. However, differences in local terrain flows when there is limited mesoscale or synoptic forces cause boundary layer flow patterns between the two locations to differ considerably. Instead, accuracy of retrievals using this approach were assessed using artificial wind fields. One set of results is presented in figure 2.

The wind field shown in figure 2a is composed of pure westerly flow from the surface to 1500 m and pure southerly flow 1500 m - 3000 m. Wind speeds start at 2.5 $m\ s^{-1}$ and increase to 5 $m\ s^{-1}$ between 500 m - 1000 m, drop back to 2.5$m\ s^{-1}$ between 1000 m - 2000 m before increasing again to 5 $m\ s^{-1}$ between 2000 m - 2500 m. Sudden wind field changes are used instead of gradual changes because sudden changes are more likely to create substantial error and frequently mark the top of the boundary layer. Large depths of uniform wind speed allow assessment of changing biases with height and retrieval disk depth. Radial velocities from the specified wind field were generated using the above equation for each azimuth-elevation pair in TSLC's scanning geometry that falls within the sampling cylinder. After those calculations, Gaussian noise is added to the calculated radial velocities to simulate observational error and turbulence. Low amplitude noise had a standard deviation of 1 $m\ s^{-1}$ and high amplitude noise had a standard deviation of 5 $m\ s^{-1}$. The data were then rounded to the nearest 0.5 $m\ s^{-1}$ to mimic truncation in level 2 radar archives. Figures 2c and 2d show the error in zonal and meridional wind components, respectively. Figure 2b shows the number of gates incorporated into regression within a particular disk. Half of the available gates at random azimuths were rejected to simulate the effect of sparse scatterers and moment filtering as described later in this section.

The retrieval performed well, even for noisy data. Errors never exceed 0.3 $m\ s^{-1}$ in either component for either series, nor does it show height dependency. The disk partitioning is well matched with the scanning geometry, roughly equally distributing gates between disks below 700 m. Above this the count of potential gates increases, but decreased scatterers aloft leaves fewer valid gates, offsetting that increase.

Prior VVP studies used the mean and first order terms of each wind component to create their regression estimates, but found that including higher order terms, when unimportant, reduced retrieval accuracy and retrieval stability (Waldteufel and Corbin 1979; Boccippio 1995; Shenghui et al. 2014). Artificial tests in this study showed that neglecting the vertical wind and higher order terms did not have a substantial impact on mean horizontal component retrieval accuracy within realistic values for unresolved terms. Thus, we chose to use only mean horizontal wind terms to maximize retrieval accuracy and stability.

Quality of data fed into the retrieval was also assessed. First, moment filters were applied, requiring reflectivity between -20 dBZ and 30 dBZ and spectrum width between 0.5 $m\ s^{-1}$ and 2 $m\ s^{-1}$. Filtering eliminates areas of significant precipitation and some vehicle traffic. Second, velocity data had to be non-zero, eliminating both weak returns and terrain blockage. Next, an outlier rejection filter is applied twice to the data (Pichugina et al. 2019; Banta et al. 2020). After this process was completed, the retrieval is run if more than 100 valid gates remain in the disk.

3. Datasets

a. TDWR Radar Network

TSLC is located on the east side of FBP (Fig. 1) and part of the larger TDWR network operated by the Federal Aviation Administration. Data from both TDWR and NEXRAD networks are archived publicly as part of the NOAA Open Data Dissemination Program, with level-2 data from TSLC available Sep 2020 - present. Since TSLC is single-pol and KMTX, northern Utah's WSR-88D, only scans far above the basin floor, dual-pol products used by Banghoff et al. (2018) are unavailable. The volume coverage pattern (VCP) for TSLC is determined automatically, switching to hazard mode upon detection of meteorological echoes greater than 20 dBZ or wind shear near the airport (Evans and Turnbull 1989). In clear air mode, TSLC scans up to 60° elevation, considerably deeper than any VCP used by a WSR-88D, and was in this mode during case studies presented later. TDWR dealiasing is handled at the data acquisition unit before transmission to end users using a multi-PRF method (Cho 2005, 2010). Since winds during the case studies stayed below the lowest possible TDWR aliasing velocity of 10 $m\ s^{-1}$, only rejected non-meteorological echoes are subject to aliasing.

b. Summer 2022 Ozone Study

The 2022 summer ozone study conducted by a UU team investigated the influence of FBP on ozone concentrations along the Wasatch Front using a network of surface observations and surface based remote sensors (McCutchan 2023). UDAQ has a number of permanently installed regulatory grade ozone monitors around the SLV and FBP basins (Fig. 1). Research grade 2B Technologies ozone monitors were placed at UUPYA, USDR4, and UFD15. Tower mounted meteorological sensors including wind and temperature were available at UUPYA and UFD15.

USDR4 and UFD15 were set up along the edge of FBP to monitor transport near the region while UUPYA monitors conditions on the playa. Ozone reported at UDAQ sites are analyzed using one-hour averages. For comparison, a one-hour running mean smoother was applied to ozone concentrations reported every 5 minutes at UU sites.

4. 2022 Labor Day Period

A strong heat wave occurred in northern Utah 29 Aug 2022 - 13 Sep 2022 and led to many days when $\overline{O_3}$ exceeded 70 ppb observed during the study period (McCutchan 2023; Jaffe et al. 2024). ”Exceedance day” refers to days where max $\overline{O_3}$ is greater than the NAAQS guideline of 70 ppb at one or more UDAQ sites, and we use ”near-exceedance day” for days with max $\overline{O_3}$ exceeding 65 ppb at a UDAQ site, the new guideline being evaluated by the EPA. Here we focus on 29 Aug - 7 Sep, referred to as the Labor Day Period (LDP). Five out of ten days were exceedance events, and every day was at least a near-exceedance event (Fig. 3). Record high temperatures and high ozone concentrations also occurred 9 - 12 Sep, however a synoptic disturbance transported wildfire smoke into northern Utah which considerably alters the air chemistry (Jaffe et al. 2024). We exclude these days to focus on clear-sky conditions.

Synoptic conditions during the LDP were quite similar between each day and matched what is often observed during other quiescent periods. Local conditions follow patterns indicating dominant thermally driven flows. In the morning, southerly down-valley flow from the Salt Lake Valley extended over FBP and an easterly jet between Weber Canyon and the northern end of Antelope Island (Chrust et al. 2013). In the afternoon, this flow reverses and becomes northwesterly through the entire region. Shortwave radiation time series from UUPYA indicate the basin lacked considerable cloud cover except during short periods during the mornings of 30 Aug and 1 Sep (not shown). Routine KSLC soundings showed typical thermodynamic conditions for weakly forced situations and were similar day-to-day. Potential temperature from the morning sounding on 6 Sep (Fig. 4) showed strong stability near the surface due to nocturnal radiative cooling, topped by a weakly stable layer. This stable layer is quickly eroded in the morning, and radiative heating leads to a superadiabatic near-surface layer and the growth of a deep CBL as seen in the evening sounding.

Figure 5 shows a composite of key datasets during the LDP. Figure 5a presents one-hour average ozone (O_3) and figure 5b shows hourly ozone concentration tendencies (O_3') computed for seven sites. Composites for the UDAQ sites were created by averaging observations for each hour. For the UU site composites, observations at the same timestamps as UDAQ observations were identified and composited following the same method. Composite O_3' was calculated from hourly differences between the UDAQ hourly reports and between the hourly smoothed data for UU sites.

The mean of all seven sites (black solid line) show common features:

- O_3 minima near sunrise (0600 - 0700 MDT);
- Increase until after solar noon (1400 MDT);
- Slow decrease in the afternoon that becomes faster over time;
- Ozone values reach low equilibrium around midnight;
- Mostly constant O_3 in the early morning hours.

This reflects the standard diurnal cycle controlled by chemical processes and boundary layer mixing under clear sky conditions as outlined in the introduction. O_3 time series for individual sites tend to fall into one of two clusters overnight: a group with below average O_3 close to FBP (USDR4, UFD15, UUPYA) and higher average O_3 in the urban region (QBV, QHW). QIP and QRP exhibit a mix of these two signals, reflecting their siting closer to the main body of the GSL and northern SLV urban area, respectively. In the morning, UFD15 tends to have higher than average O_3 and overall the greatest daily amplitude, while UUPYA and USDR4 consistently have lower O_3. UUPYA's distance from pollution sources likely explains lower O_3, and VOC emissions from a waste treatment plant near USDR4 may have locally altered the air chemistry. Jaffe et al. (2024) show mean diurnal cycles of O_3, NO_x, and VOCs at QHW Aug-Sep 2022. As expected, the NO_x and VOC diurnal variations are opposite those of O_3 with peak concentrations prior to sunrise and lowest concentrations during the afternoon.

Composite VVP winds for the LDP are shown in figure 5c. VVPs were averaged in height along the native logarithmic axis and time bins of 18 minutes, corresponding to roughly 3 volume scans. Zonal and meridional wind components were averaged to derive composite direction while wind speed was averaged separately.

Near sunrise at 0630 MDT, flow near the surface is initially stalled, but a layer of northwesterly flow develops and begins deepening through the morning, coinciding with the initial growth of the CBL. The flow at 200m and aloft is more coupled with the terrain wind system and transitions from southeasterly to easterly. At 1000 MDT, flow below 400m transitions from northeasterly to northwesterly, following the local slope flow and playa breeze transitioning to the upslope and onshore phases of their diurnal cycles. Above the shear layer at 400 m marking the top of the CBL at 1000 MDT, flow transitions from easterly to southerly. From 1000 MDT - 1300 MDT, the shear layer moves from 400 m to above the top of the profile, marking rapid CBL growth. By 1400 MDT, flow through the entire profile is northwesterly with nearly uniform speed, coinciding with the up-valley phase of the thermally driven flow and deep momentum transport. Near sunset (2000 MDT), flow through the depth of the profile shifts from northwesterly to northeasterly and becomes decoupled from the surface. This northwesterly flow dissipates from the bottom up overnight, fully dissipating by 0300 MDT. Meanwhile, at 2230 MDT, weak southerly flow develops in a layer near the surface and persists with the northeasterly flow, becoming westerly at 0300 MDT until sunrise at 0600 MDT.

Composite mean reflectivity RD-QVPs (Fig. 5d) appear similar to profiles in prior literature. Beginning at 0800 MDT, an area of increased reflectivity appears at the surface, deepening in step with boundary layer flow seen in the VVP. It reaches its peak depth at 1000 MDT, when the flow reversal occurs, then slowly decreases through the afternoon hours as scatterers are dispersed through the deepening boundary layer. Reflectivity then increases twice in the evening, the first time due to bird activity near the radar and the second time due to solar effects. A similar increase in reflectivity happens near 0630 MDT corresponding with sunrise.

While synoptic conditions were fairly similar through the LDP, subtle differences were present in the vertical wind profile each day. On 6 Sep, easterly flow aloft was stronger and more persistent than the composite (Fig. 6c). Easterly flow in this region corresponds to downslope flow, which typically displaces high ozone concentrations from the prior day's CBL and replaces them with comparatively lower background ozone concentrations overnight during clear-sky high ozone events. As the CBL grows during the following day, decreased ozone concentrations aloft cause a diluting fumigation effect.

Despite being one of the warmest days of the period, 6 Sep had some of the lowest observed $\overline{O_3}$ (Fig. 3). This enhanced easterly flow may indicate increased clearing of the residual layer by downslope flow, lowering surface ozone more than usual as the CBL grew in turn. The enhanced dilution effect can also be seen in the O_3' observations, where O_3' was lower than average during the morning hours and more negative during the afternoon compared to composite (Fig. 6b). Persistent easterly flow and reduced ozone concentrations (Fig. 3) were also present on 5 Sep (not shown).

5. Discussion and Summary

Clear air returns from weather radars can be used to derive boundary layer wind fields at high temporal and vertical resolution. QVPs and VADs can be used to construct vertical profiles of radar moments and horizontal winds above the radar, but assume the area near the radar is horizontally uniform. In complex terrain, areas meeting this assumption are limited in size, thus retrievals from a single conical scan must be rejected at a lower height. By combining multiple conical scans, retrieval vertical resolution and maximum depth can be improved.

This study applied an under-utilized resource to examine the boundary layer: output from the TSLC TDWR. This single-pol radar is located close to the basin floor and samples in higher spatial and temporal resolution than the nearby WSR-88D but is affected by increased terrain blockage. The VVP and RD-QVP retrievals using a 5 km radius were used to observe the boundary layer during a high ozone period. Retrieval disks were partitioned along a logarithmic height axis to enhance near-surface resolution. Limitations of retrieval accuracy with this geometry were assessed using artificial wind fields, which found that retrievals remained highly accurate, even when using noisy data.

Tropospheric ozone is a significant environmental hazard regulated by the EPA, and the northern Wasatch Front is in moderate non-attainment of the $\overline{O_3}$ standard. Thermally driven circulations from nearby mountains, lake breezes, and playa breezes substantially impact ozone concentrations in this region. VVP and RD-QVP retrievals during an unusually high ozone period were calculated from TSLC and provided an unprecedented view of these processes. Shear layers frequently developed near the surface briefly after sunrise and increased in height throughout the day, yielding uniform flow through the depth of the profile in the afternoon. A reversal from off-shore to onshore flows is present in the morning, likely corresponding to reversal of local thermally driven circulations. Flow profiles of individual days revealed flow interactions with the terrain that may have contributed to subtle differences in peak ozone concentrations. The shear layer matched reflectivity-derived boundary layer height estimates, which saw peak reflectivity near the time of flow reversal. The estimates diverged in the afternoon as deep turbulent mixing dispersed scatterers within the CBL and decreased reflectivity.

TSLC has been used in this and prior studies to provide a more complete view of boundary layer processes relevant to air-quality. Many other cities throughout the Intermountain West are also in non-attainment of EPA standards and are similarly influenced by flows in complex terrain. TDWRs located in Phoenix, Las Vegas, and Denver may provide further insights into thermally driven flows' influence upon air quality by applying these retrieval methods. Retrievals with limited radius can similarly be applied to study boundary layer processes with short horizontal length scales using any operational scanning radar. Utility of retrievals from TDWR may be limited in the winter months because of a lack of scatterers, in which case the differential reflectivity QVP method outlined in Banghoff et al. (2018) may be a better choice. However, WSR-88D radars in the west offering this product may struggle to capture key details due to high altitude siting locations and shallow clear-air coverage patterns.

Acknowledgments. The authors would like to thank Alex Jacques for assistance with processing surface meteorological and ozone data during the summer ozone project. We would also like to thank Colin Johnson for maintaining field study equipment and creating the figure outlining key sites. This work was possible due to the computing resources provided by the University of Utah's Center for High Performance Computing. The Python ARM Radar Toolkit (`Py_ART`) library was used extensively for radar data processing. Funding for this project was provided by the Utah Division of Air Quality and the NOAA/National Weather Service Collaborative Science, Technology, and Applied Research (CSTAR) Program, Award NA20NWS468046.

Data availability statement. Radar data used in this study are available from cloud providers as part of the NOAA Open Data Dissemination program.

References

Bachmann, S., and D. Zrnić, 2007: Spectral density of polarimetric variables separating biological scatterers in the VAD display. *J. Atmos. Oceanic Technol.*, **24 (7)**, 1186–1198, https://doi.org/10.1175/JTECH2043.1.

Baier, B. C., W. H. Brune, B. L. Lefer, D. O. Miller, and D. K. Martins, 2015: Direct ozone production rate measurements and their use in assessing ozone source and receptor regions for Houston in 2013. *Atmospheric Environment*, **114**, 83–91, https://doi.org/https://doi.org/10.1016/j.atmosenv.2015.05.033.

Banghoff, J. R., D. J. Stensrud, and M. R. Kumjian, 2018: Convective boundary layer depth estimation from S-Band dual-polarization radar. *J. Atmos. Oceanic Technol.*, **35 (8)**, 1723–1733, https://doi.org/10.1175/JTECH-D-17-0210.1.

Banta, R. M., and Coauthors, 2011: Dependence of daily peak O_3 concentrations near Houston, Texas on environmental factors: Wind speed, temperature, and boundary-layer depth. *Atmos. Environ.*, **45 (1)**, 162–173, https://doi.org/10.1016/j.atmosenv.2010.09.030.

Banta, R. M., and Coauthors, 2020: Characterizing NWP model errors using Doppler-lidar measurements of recurrent regional diurnal flows: Marine-air intrusions into the Columbia River Basin. *Mon. Wea. Rev.*, **148 (3)**, 929–953, https://doi.org/10.1175/MWR-D-19-0188.1.

Bian, H., J. Min, and F. Shen, 2023: Application of radar radial velocity data assimilation in the forecasts of typhoon linfa based on different horizontal length scale factors. *Atmosphere*, **14 (3)**, https://doi.org/10.3390/atmos14030582.

Blaylock, B. K., J. D. Horel, and E. T. Crosman, 2017: Impact of lake breezes on summer ozone concentrations in the Salt Lake Valley. *J. Appl. Meteor. Climatol.*, **56 (2)**, 353–370, https://doi.org/10.1175/JAMC-D-16-0216.1.

Boccippio, D. J., 1995: A diagnostic analysis of the VVP single-doppler retrieval technique. *J. Atmos. Oceanic Technol.*, **12 (2)**, 230–248, https://doi.org/10.1175/1520-0426(1995)012⟨0230:ADAOTV⟩2.0.CO;2.

Brodin, M., D. Helmig, and S. Oltmans, 2010: Seasonal ozone behavior along an elevation gradient in the Colorado Front Range Mountains. *Atmos. Environ.*, **44 (39)**, 5305–5315, https://doi.org/10.1016/j.atmosenv.2010.06.033.

Browning, K. A., and R. Wexler, 1968: The determination of kinematic properties of a wind field using Doppler radar. *J. Appl. Meteor. Climatol.*, **7 (1)**, 105–113, https://doi.org/10.1175/1520-0450(1968)007⟨0105:TDOKPO⟩2.0.CO;2.

Chandrasekar, V., R. M. Beauchamp, and R. Bechini, 2023: *Introduction to Dual Polarization Weather Radar: Fundamentals, Applications, and Networks*. Cambridge University Press.

Cho, J. Y. N., 2005: Multi-PRI signal processing for the Terminal Doppler Weather Radar. Part II: Range–velocity ambiguity mitigation. *J. Atmos. Oceanic Technol.*, **22 (10)**, 1507–1519, https://doi.org/10.1175/JTECH1805.1.

Cho, J. Y. N., 2010: Signal processing algorithms for the Terminal Doppler Weather Radar: Build 2. Tech. Rep. ATC-363, MIT Lincoln Laboratory. 89 pp.

Chow, F. K., S. F. De Wekker, and B. J. Snyder, Eds., 2013: *Mountain Weather Research and Forecasting: Recent Progress and Current Challenges*, 261–289. Springer Netherlands, Dordrecht, https://doi.org/10.1007/978-94-007-4098-3_5, URL https://doi.org/10.1007/978-94-007-4098-3_5.

Chrust, M. F., C. D. Whiteman, and S. W. Hoch, 2013: Observations of thermally driven wind jets at the exit of Weber Canyon, Utah. *J. Appl. Meteor. Climatol.*, **52 (5)**, 1187–1200, https://doi.org/10.1175/JAMC-D-12-0221.1.

Clifton, O. E., and Coauthors, 2020: Dry deposition of ozone over land: Processes, measurement, and modeling. *Rev. Geophys.*, **58 (1)**, e2019RG000 670, https://doi.org/10.1029/2019RG000670.

Coates, J., K. A. Mar, N. Ojha, and T. M. Butler, 2016: The influence of temperature on ozone production under varying no$_x$ conditions – a modelling study. *Atmospheric Chemistry and Physics*, **16 (18)**, 11 601–11 615, https://doi.org/10.5194/acp-16-11601-2016.

Crosman, E. T., and J. D. Horel, 2016: Winter lake breezes near the great salt lake. *Boundary Layer Meteorol.*, **159 (2)**, 439–464, https://doi.org/10.1007/s10546-015-0117-6.

Davison, J. L., R. M. Rauber, and L. D. Girolamo, 2013: A revised conceptual model of the tropical marine boundary layer. part ii: Detecting relative humidity layers using bragg scattering from s-band radar. *Journal of the Atmospheric Sciences*, **70 (10)**, 3025 – 3046, https://doi.org/10.1175/JAS-D-12-0322.1.

De Wekker, S. F. J., and M. Kossmann, 2015: Convective boundary layer heights over mountainous terrain—a review of concepts. *Frontiers in Earth Science*, **3**, https://doi.org/10.3389/feart.2015.00077.

Doviak, R. J., and D. S. Zrnic, 1993: *Doppler Weather Radar and Weather Observations*. 2nd ed., Dover Publications, Inc., 562 pp.

Elmore, K. L., P. L. Heinselman, and D. J. Stensrud, 2012: Using wsr-88d data and insolation estimates to determine convective boundary layer depth. *Journal of Atmospheric and Oceanic Technology*, **29 (4)**, 581 – 588, https://doi.org/10.1175/JTECH-D-11-00043.1.

Evans, J., and D. Turnbull, 1989: Development of an automated windshear detection system using doppler weather radar. *Proceedings of the IEEE*, **77 (11)**, 1661–1673, https://doi.org/10.1109/5.47729.

Fann, N., A. D. Lamson, S. C. Anenberg, K. Wesson, D. Risley, and B. J. Hubbell, 2012: Estimating the national public health burden associated with exposure to ambient pm2.5 and ozone. *Risk Analysis*, **32 (1)**, 81–95, https://doi.org/https://doi.org/10.1111/j.1539-6924.2011.01630.x.

Gao, J., M. Xue, and D. J. Stensrud, 2013: The development of a hybrid enkf-3dvar algorithm for storm-scale data assimilation. *Advances in Meteorology*, **2013 (512656)**, https://doi.org/https://doi.org/10.1155/2013/512656.

Griffin, E. M., T. J. Schuur, and A. V. Ryzhkov, 2018: A polarimetric analysis of ice microphysical processes in snow, using quasi-vertical profiles. *J. Appl. Meteor. Climatol.*, **57 (1)**, 31 – 50, https://doi.org/10.1175/JAMC-D-17-0033.1.

Heinselman, P. L., P. L. Spencer, K. L. Elmore, D. J. Stensrud, R. M. Hluchan, and P. C. Burke, 2009: Radar reflectivity–based estimates of mixed layer depth. *J. Atmos. Oceanic Technol.*, **26 (2)**, 229–239, https://doi.org/10.1175/2008JTECHA1091.1.

Holleman, I., 2005: Quality control and verification of weather radar wind profiles. *J. Atmos. Oceanic Technol.*, **22 (10)**, 1541–1550, https://doi.org/10.1175/JTECH1781.1.

Horel, J., E. Crosman, A. Jacques, B. Blaylock, S. Arens, A. Long, J. Sohl, and R. Martin, 2016: Summer ozone concentrations in the vicinity of the great salt lake. *Atmospheric Science Letters*, **17 (9)**, 480–486, https://doi.org/10.1002/asl.680.

Hu, J., and A. Ryzhkov, 2022: Climatology of the vertical profiles of polarimetric radar variables and retrieved microphysical parameters in continental/tropical MCSs and landfalling hurricanes. *J. Geophys. Res.*, **127 (5)**, e2021JD035 498, https://doi.org/10.1029/2021jd035498.

Hubbell, B. J., A. Hallberg, D. R. McCubbin, and E. Post, 2005: Health-related benefits of attaining the 8-hr ozone standard. *Environmental Health Perspectives*, **113 (1)**, 73–82, https://doi.org/10.1289/ehp.7186.

Jaffe, D., 2011: Relationship between surface and free tropospheric ozone in the western u.s. *Environmental Science & Technology*, **45 (2)**, 432–438, https://doi.org/10.1021/es1028102.

Jaffe, D. A., and Coauthors, 2024: Key results from the salt lake regional smoke, ozone, and aerosol study (SAMOZA). *Journal of the Air & Waste Management Association*, **74 (3)**, 163–180, https://doi.org/10.1080/10962247.2024.2301956.

Kaser, L., and Coauthors, 2017: The effect of entrainment through atmospheric boundary layer growth on observed and modeled surface ozone in the colorado front range. *Journal of Geophysical Research: Atmospheres*, **122 (11)**, 6075–6093, https://doi.org/https://doi.org/10.1002/2016JD026245.

Lehner, M., and M. W. Rotach, 2018: Current challenges in understanding and predicting transport and exchange in the atmosphere over mountainous terrain. *Atmosphere*, **9 (7)**, https://doi.org/10.3390/atmos9070276.

Liu, S. C., and Coauthors, 1992: A study of the photochemistry and ozone budget during the Mauna Loa Observatory Photochemistry Experiment. *J. Geophys. Res. Atmos.*, **97 (D10)**, 10 463–10 471, https://doi.org/10.1029/91JD02298.

Logan, J. A., M. J. Prather, S. C. Wofsy, and M. B. McElroy, 1981: Tropospheric chemistry: A global perspective. *Journal of Geophysical Research: Oceans*, **86 (C8)**, 7210–7254, https://doi.org/https://doi.org/10.1029/JC086iC08p07210.

Massey, J. D., W. J. Steenburgh, S. W. Hoch, and D. D. Jensen, 2017: Simulated and observed surface energy fluxes and resulting playa breezes during the MATERHORN field campaigns. *J. Appl. Meteor. Climatol.*, **56 (4)**, 915–935, https://doi.org/10.1175/JAMC-D-16-0161.1.

Matejka, T., and R. C. Srivastava, 1991: An improved version of the extended velocity-azimuth display analysis of single-Doppler radar data. *J. Atmos. Oceanic Technol.*, **8 (4)**, 453–466, https://doi.org/10.1175/1520-0426(1991)008⟨0453:AIVOTE⟩2.0.CO;2.

McClure, C. D., and D. A. Jaffe, 2018: Investigation of high ozone events due to wildfire smoke in an urban area. *Atmospheric Environment*, **194**, 146–157, https://doi.org/https://doi.org/10.1016/j.atmosenv.2018.09.021.

McCutchan, A. C., 2023: Terminal Doppler Weather Radar boundary layer observations during a summer high ozone period in complex terrain. M.S. thesis, Department of Atmospheric Sciences, University of Utah.

Melnikov, V. M., R. J. Doviak, D. S. Zrnić, and D. J. Stensrud, 2011: Mapping bragg scatter with a polarimetric wsr-88d. *Journal of Atmospheric and Oceanic Technology*, **28 (10)**, 1273 – 1285, https://doi.org/https://doi.org/10.1175/JTECH-D-10-05048.1.

Melnikov, V. M., R. J. Doviak, D. S. Zrnić, and D. J. Stensrud, 2013: Structures of bragg scatter observed with the polarimetric wsr-88d. *Journal of Atmospheric and Oceanic Technology*, **30 (7)**, 1253 – 1258, https://doi.org/10.1175/JTECH-D-12-00210.1.

Ninneman, M., and D. A. Jaffe, 2021: The impact of wildfire smoke on ozone production in an urban area: Insights from field observations and photochemical box modeling. *Atmospheric Environment*, **267**, 118 764, https://doi.org/https://doi.org/10.1016/j.atmosenv.2021.118764.

Pichugina, Y. L., and Coauthors, 2019: Spatial variability of winds and HRRR–NCEP model error statistics at three Doppler-lidar sites in the wind-energy generation region of the Columbia River Basin. *J. Appl. Meteor. Climatol.*, **58 (8)**, 1633–1656, https://doi.org/10.1175/JAMC-D-18-0244.1.

Pusede, S. E., A. L. Steiner, and R. C. Cohen, 2015: Temperature and recent trends in the chemistry of continental surface ozone. *Chemical Reviews*, **115 (10)**, 3898–3918, https://doi.org/10.1021/cr5006815.

Rabin, R. M., and R. J. Doviak, 1989: Meteorological and astronomical influences on radar reflectivity in the convective boundary layer. *Journal of Applied Meteorology and Climatology*, **28 (11)**, 1226 – 1235, https://doi.org/10.1175/1520-0450(1989)028⟨1226:MAAIOR⟩2.0.CO;2.

Richardson, L. M., J. G. Cunningham, W. D. Zittel, R. R. Lee, R. L. Ice, V. M. Melnikov, N. P. Hoban, and J. G. Gebauer, 2017: Bragg scatter detection by the wsr-88d. part i: Algorithm development. *Journal of Atmospheric and Oceanic Technology*, **34 (3)**, 465 – 478, https://doi.org/10.1175/JTECH-D-16-0030.1.

Rickly, P. S., and Coauthors, 2023: Influence of Wildfire on Urban Ozone: An Observationally Constrained Box Modeling Study at a Site in the Colorado Front Range. *Environmental Science & Technology*, **57 (3)**, 1257–1267, https://doi.org/10.1021/acs.est.2c06157.

Ryzhkov, A., P. Zhang, H. Reeves, M. Kumjian, T. Tschallener, S. Trömel, and C. Simmer, 2016: Quasi-vertical profiles—A new way to look at polarimetric radar data. *J. Atmos. Oceanic Technol.*, **33 (3)**, 551–562, https://doi.org/10.1175/JTECH-D-15-0020.1.

Seinfeld, J. H., and S. N. Pandis, 2016: *Atmospheric chemistry and physics: from air pollution to climate change*. 3rd ed., Wiley, New York.

Shenghui, Z., W. Ming, W. Lijun, Z. Chang, and Z. Mingxu, 2014: Sensitivity analysis of the VVP wind retrieval method for single-Doppler weather radars. *J. Atmos. Oceanic Technol.*, **31 (6)**, 1289–1300, https://doi.org/10.1175/JTECH-D-13-00190.1.

Simpson, W. R., and Coauthors, 2007: Halogens and their role in polar boundary-layer ozone depletion. *Atmospheric Chemistry and Physics*, **7 (16)**, 4375–4418, https://doi.org/10.5194/acp-7-4375-2007.

Sousa, S. I. V., M. C. M. Alvim-Ferraz, and F. G. Martins, 2013: Health effects of ozone focusing on childhood asthma: What is now known – a review from an epidemiological point of view. *Chemosphere*, **90 (7)**, 2051–2058, https://doi.org/10.1016/j.chemosphere.2012.10.063.

Teschke, G., and V. Lehmann, 2017: Mean wind vector estimation using the velocity–azimuth display (VAD) method: An explicit algebraic solution. *Atmos. Meas. Tech.*, **10 (9)**, 3265–3271, https://doi.org/10.5194/amt-10-3265-2017.

Tobin, D. M., and M. R. Kumjian, 2017: Polarimetric radar and surface-based precipitation-type observations of ice pellet to freezing rain transitions. *Wea. Forecasting*, **32 (6)**, 2065–2082, https://doi.org/10.1175/WAF-D-17-0054.1.

Tong, C.-C., Y. Jung, M. Xue, and C. Liu, 2020: Direct assimilation of radar data with ensemble kalman filter and hybrid ensemble-variational method in the national weather service operational data assimilation system gsi for the stand-alone regional fv3 model at a convection-allowing resolution. *Geophysical Research Letters*, **47 (19)**, e2020GL090 179, https://doi.org/https://doi.org/10.1029/2020GL090179, https://agupubs.onlinelibrary.wiley.com/doi/pdf/10.1029/2020GL090179.

Waldteufel, P., and H. Corbin, 1979: On the analysis of single-doppler radar data. *J. Appl. Meteor. Climatol.*, **18 (4)**, 532–542, https://doi.org/10.1175/1520-0450(1979)018⟨0532:OTAOSD⟩2.0.CO;2.

Wang, Y., and Z. Pu, 2021: Assimilation of radial velocity from coastal nexrad into hwrf for improved forecasts of landfalling hurricanes. *Weather and Forecasting*, **36 (2)**, 587 – 599, https://doi.org/10.1175/WAF-D-20-0163.1.

Wildmann, N., E. Päschke, A. Roiger, and C. Mallaun, 2020: Towards improved turbulence estimation with Doppler wind lidar velocity-azimuth display (VAD) scans. *Atmos. Meas. Tech.*, **13 (8)**, 4141–4158, https://doi.org/10.5194/amt-13-4141-2020.

Xiao, Q., Y.-H. Kuo, J. Sun, W.-C. Lee, E. Lim, Y.-R. Guo, and D. M. Barker, 2005: Assimilation of doppler radar observations with a regional 3dvar system: Impact of doppler velocities on forecasts of a heavy rainfall case. *Journal of Applied Meteorology*, **44 (6)**, 768 – 788, https://doi.org/10.1175/JAM2248.1.

Xu, L., and Coauthors, 2021: Ozone chemistry in western u.s. wildfire plumes. *Science Advances*, **7 (50)**, eabl3648, https://doi.org/10.1126/sciadv.abl3648, https://www.science.org/doi/pdf/10.1126/sciadv.abl3648.

Zrnic, D., and A. Ryzhkov, 1998: Observations of insects and birds with a polarimetric radar. *IEEE Trans. Geosci. Remote Sens.*, **36 (2)**, 661–668, https://doi.org/10.1109/36.662746.

Zumpfe, D. E., and J. D. Horel, 2007: Lake-breeze fronts in the salt lake valley. *J. Appl. Meteor. Climatol.*, **46 (2)**, 196–211, https://doi.org/10.1175/JAM2449.1.

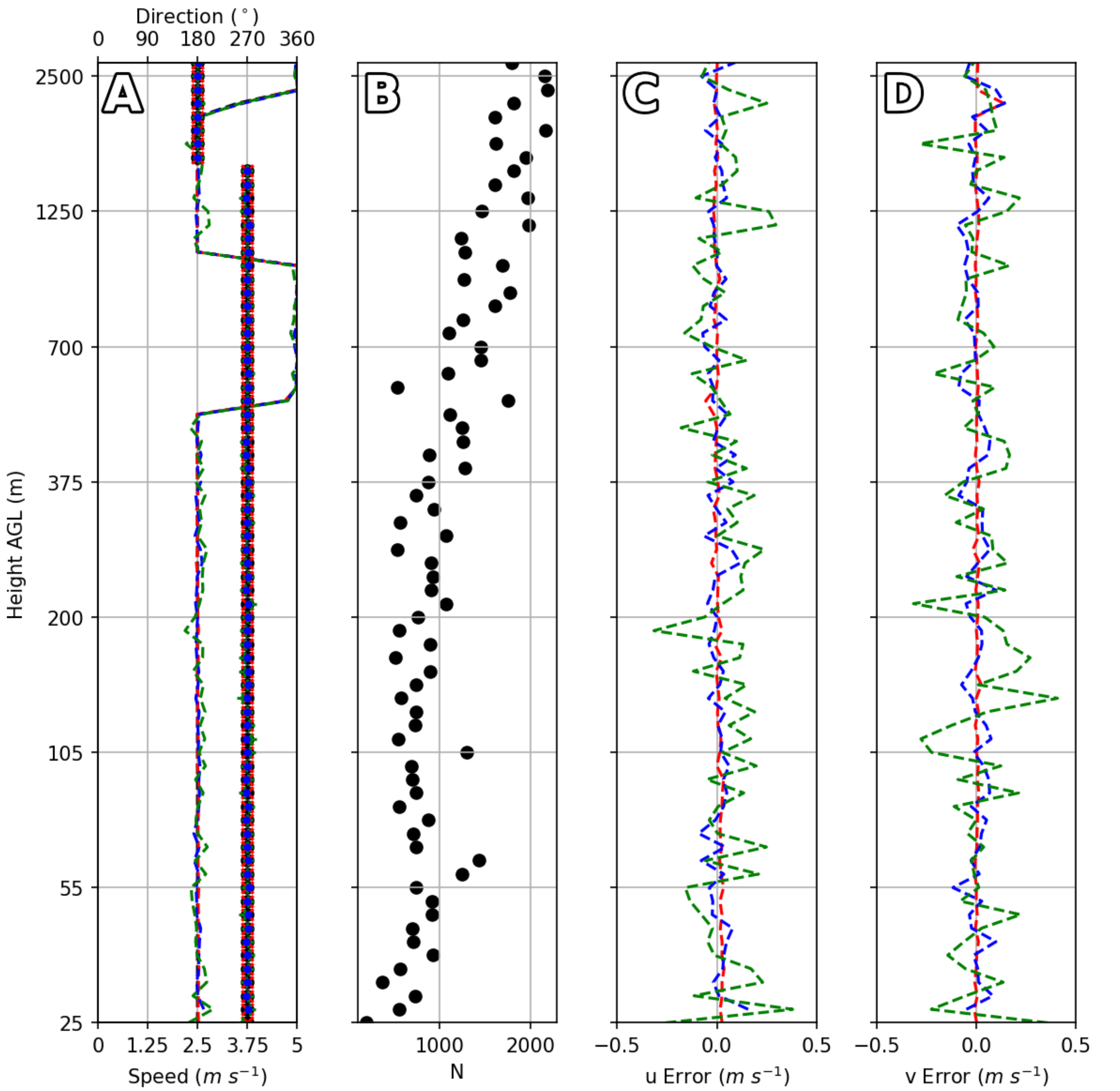

167 FIG. 2. Example of a VVP test using study retrieval geometry. Red series indicates retrieval when computed
168 radial velocities are rounded to the nearest 0.5 $m\ s^{-1}$, blue indicates results when white noise with a standard
169 deviation of 1 $m\ s^{-1}$ is applied before rounding, and green indicates results when white noise standard deviation
170 is 5 $m\ s^{-1}$. (a) Wind speed and direction profiles used for testing and retrieval recreation on a logarithmic height
171 axis. Black series indicates expected results. Lines indicate wind speed ($m\ s^{-1}$), while symbols indicate wind
172 direction (degrees). (b) Number of gates included in retrieval disks. (c) Zonal component error ($m\ s^{-1}$). (d) As
173 in (c) for meridional component.

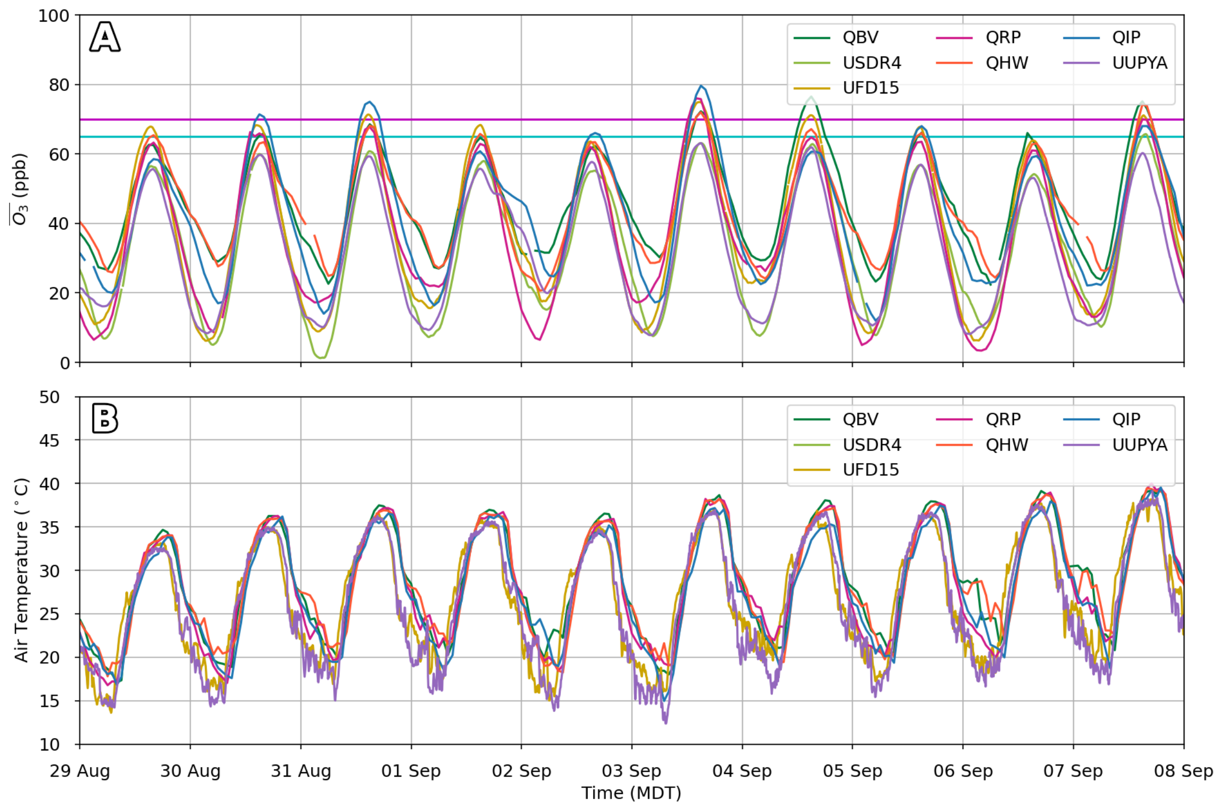

FIG. 3. Surface station observations from study sites during the LDP. (a) Timeseries of $\overline{O_3}$ (ppb). $\overline{O_3}$ values are computed from hourly (5 min) observations at UDAQ (UU) sites, respectively. Magenta line indicates present 70 ppb NAAQS $\overline{O_3}$ standard, and cyan line indicates proposed 65 ppb standard. (b) As in (a) except for air temperature (C°) at hourly (5 min) intervals at UDAQ (UU) sites, respectively.

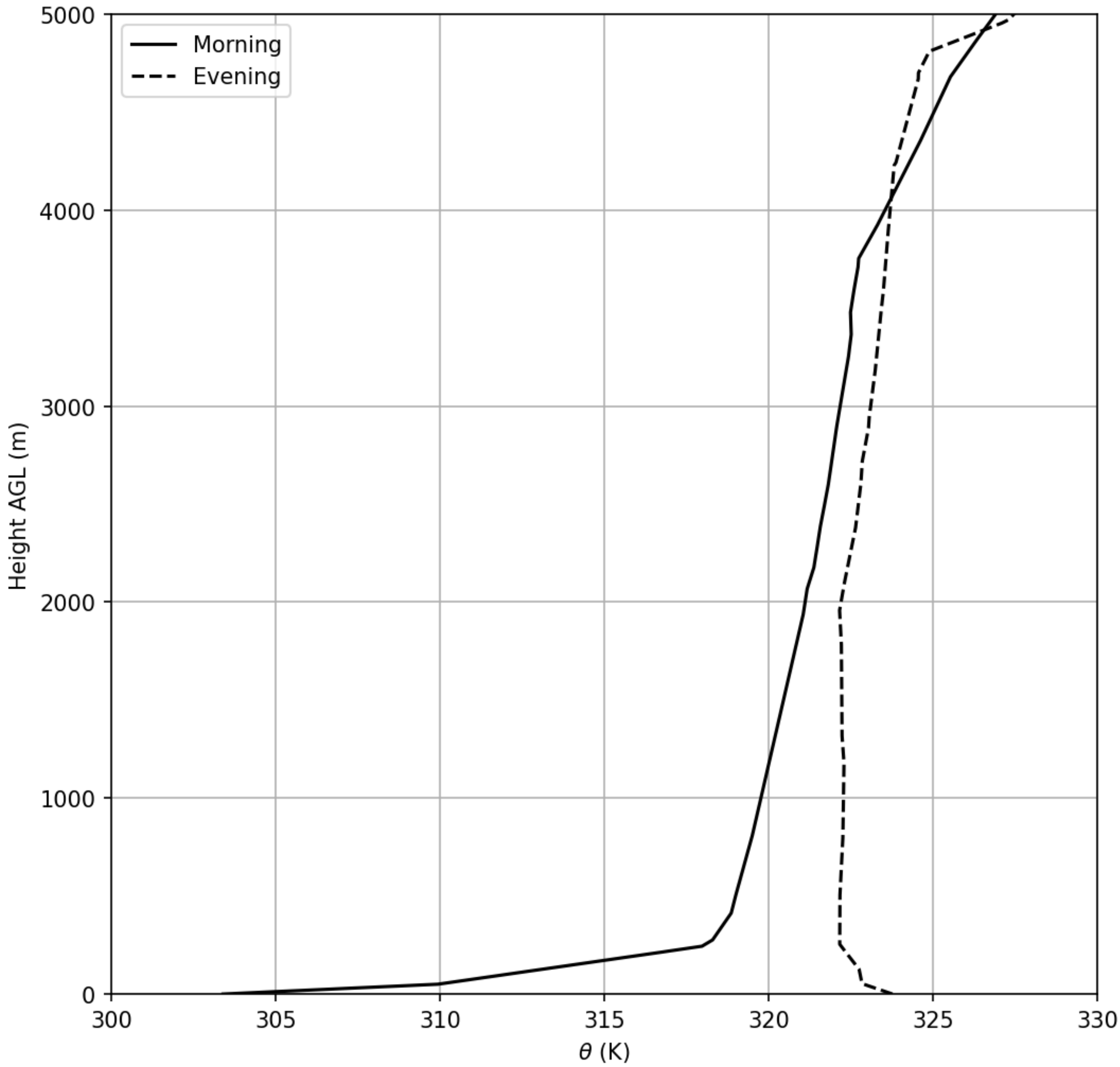

Fig. 4. Potential temperature (K) profiles derived from KSLC soundings on 6 Sep. Solid line indicates profile during the morning (12 UTC/06 MDT) sounding, and dashed line indicates profile from evening (00 UTC/18 MDT) sounding.

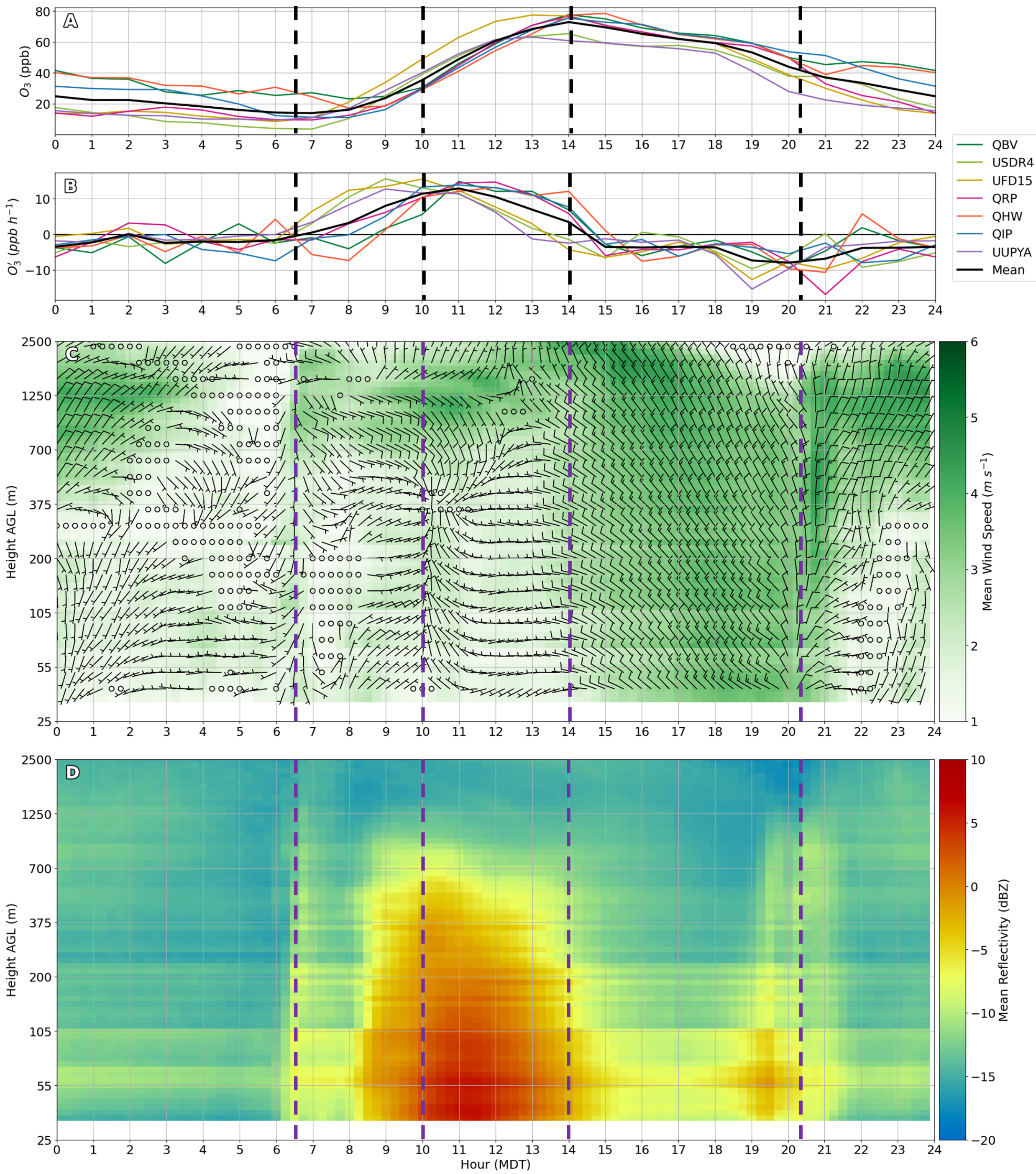

FIG. 5. Composite of observations made during the ten-day LDP. Dashed lines indicate times of interest in analysis. (a) Composite O_3 (ppb) computed within the LDP of UDAQ observations during each hour and hourly running mean observations at UU sites. (b) As in (a) except for O_3' (c) Composite TSLC VVP computed over native logarithmic height axis and 18 minute intervals (shaded, $m\ s^{-1}$) and wind barbs during the LDP. Half (full) barbs correspond to horizontal wind of 1.25 (2.5) $m\ s^{-1}$. Every third barb in height is plotted.(d) As in (c) except for composite TSLC mean reflectivity RD-QVP (dBZ).

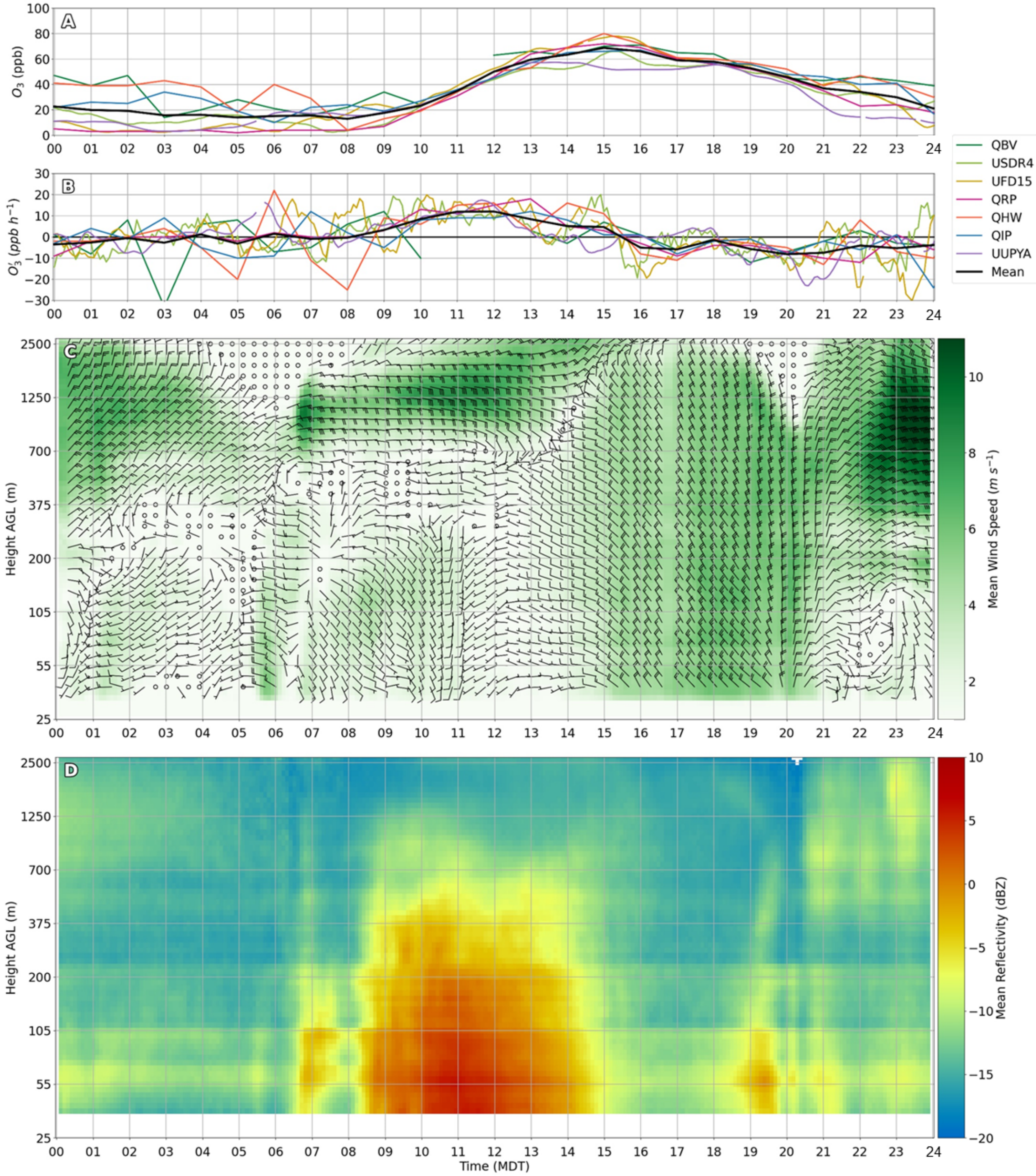

FIG. 6. Surface observations and radar retrievals 06 Sep 2022. (a) O_3 (ppb) from UDAQ and UU sites. (b) as in (a) except for O_3'. (c) TSLC VVP wind speed (fill) and subsampled wind barbs during 06 Sep 2022. Half (full) barbs correspond to horizontal wind speed of 1.25 (2.5) $m\ s^{-1}$. Every second barb in time and third barb in height is shown. (d) TSLC mean reflectivity RD-QVP (dBZ) during 06 Sep 2022.